

Article

# Electrochemical reduction of CO to liquid C<sub>2+</sub> with high Faradaic efficiency of amorphous CuO hybrid material wrapped in carbon and silica

Yue-Xia Yang<sup>1</sup>, Zhen-Hong He<sup>1,\*</sup>, Hui-Hui Cao<sup>1</sup>, Yong-Chang Sun<sup>1</sup>, Yue Tian<sup>1</sup>, Jiajie Liu<sup>1</sup>, Weitao Wang<sup>1</sup>, Huan Wang<sup>1</sup>, Yang Yang<sup>1</sup>, Zhao-Tie Liu<sup>1,2,\*</sup>

<sup>1</sup> Shaanxi Key Laboratory of Chemical Additives for Industry, College of Chemistry and Chemical Engineering, Shaanxi University of Science and Technology, Xi'an 710021, Shaanxi Province, China

<sup>2</sup> School of Chemistry and Chemical Engineering, Shaanxi Normal University, Xi'an 710119, Shaanxi Province, China

\* Corresponding authors: Zhen-Hong He, [hezhenhong@sust.edu.cn](mailto:hezhenhong@sust.edu.cn); Zhao-Tie Liu, [ztliu@snnu.edu.cn](mailto:ztliu@snnu.edu.cn)

## CITATION

Yang YX, He ZH, Cao HH, et al. Electrochemical reduction of CO to liquid C<sub>2+</sub> with high Faradaic efficiency of amorphous CuO hybrid material wrapped in carbon and silica. *Clean Energy Science and Technology*. 2024; 2(2): 132. <https://doi.org/10.18686/cest.v2i2.132>

## ARTICLE INFO

Received: 20 February 2024  
Accepted: 9 April 2024  
Available online: 26 April 2024

## COPYRIGHT



Copyright © 2024 by author(s). *Clean Energy Science and Technology* is published by Universe Scientific Publishing. This work is licensed under the Creative Commons Attribution (CC BY) license. <https://creativecommons.org/licenses/by/4.0/>

**Abstract:** Carbon monoxide (CO) is well recognized as one of the key intermediates for carbon dioxide (CO<sub>2</sub>) electrolytic reduction to C<sub>2+</sub> products, which has been a hot research field recently. Developing an efficient catalyst that focuses on achieving C-C coupling is highly important for the production of C<sub>2+</sub> products. In the present work, we present a feasible approach via the combination of electrostatic assembly and the hydrothermal method of coupling silicon polyanions and copper salts to build an amorphous copper hybrid material wrapped in carbon-silica, denoted as CuO@C-SiO<sub>2</sub>-X (where X means preparation temperature), as an efficient electrocatalyst for carbon monoxide reduction mainly to liquid C<sub>2+</sub> products. The CuO@C-SiO<sub>2</sub>-X catalyst demonstrated excellent electrocatalytic activity and selectivity, especially to C<sub>2+</sub> liquid products with the highest Faradaic efficiency of 81.5%. Additionally, the catalyst showed good stability. The presence of carbon enhanced electronic conductivity, and the silica protected the amorphous CuO from aggregation into crystalline structures. The present work not only provides an efficient catalyst for CO electrocatalytic reduction to liquid C<sub>2+</sub> chemicals but also offers a protocol for building Cu-based catalysts with high selectivity to C<sub>2+</sub> products in CO reduction.

**Keywords:** carbon monoxide; electroreduction; C<sub>2+</sub> products; Cu-based catalyst; silica

## 1. Introduction

Electrochemical reduction of carbon dioxide (CO<sub>2</sub>) to produce valuable chemicals and fuels is a promising avenue for mitigating CO<sub>2</sub> emissions and utilizing renewable energy sources. This process has the potential to convert CO<sub>2</sub> into high-value-added products, thereby helping to address climate change and contribute to a more sustainable energy economy [1]. Among the produced chemicals, C<sub>2+</sub> products with higher energy density and more value compared with those of C<sub>1</sub> products, such as methane (CH<sub>4</sub>), carbon monoxide (CO), etc., have attracted much attention during the last decade. However, the formation of C<sub>2+</sub> products involves the reduction of carbon dioxide and the processes of the coupling of C-C, which are difficult to realize. To enhance the efficiency of CO<sub>2</sub> reduction reactions (CO<sub>2</sub>RR) for the production of high-value multi-carbon products, significant advancements have been made in designing efficient catalysts, suitable electrolytes, and electrochemical set-ups, etc., to enhance the catalytic activity, electrical conductivity, mass transfer, and gas adsorption, etc. [2–6]. However, one main focus is on developing efficient catalysts to achieve CO<sub>2</sub> reduction and C-C coupling.

Generally, it is well known that the formation of  $C_{2+}$  products of electrocatalytic  $CO_2$  reduction processes involves a CO intermediate. CO itself is an abundant and cost-effective C1 resource in industries [7,8]. Developing efficient catalytic systems for the CO electrochemical conversion into  $C_{2+}$  products is highly important both in  $CO_2$  electrochemical reduction ( $CO_2ER$ ) and CO electrochemical reduction (COER). Especially, developing efficient catalysts for CO electrochemical reduction will provide a special insight into addressing challenges related to undesirable side reactions or low selectivity that may occur when utilizing  $CO_2$  in electrochemical processes. Indeed, COER, particularly when utilizing renewable electricity and operating in aqueous electrolytes, has garnered significant attention due to its several advantages. These advantages include a simple and convenient operation, the ease of controlling reaction conditions, and the adjustable structure of electrolytic cells. This has made COER an attractive research area for producing valuable chemicals and fuels.

Similar to  $CO_2ER$ , in COER, copper-based catalysts have shown their capabilities to convert CO into valuable multi-carbon products, comprising a combination of gaseous ethylene and liquid  $C_{2+}$  products [9–11]. Liquid  $C_{2+}$  products have garnered significant interest owing to their superior energy density and high added value compared with those of C1 gaseous products [12]. Efforts have been made to promote the formation of  $C_{2+}$  products through different means, including the implementation of engineered copper sections [10,13], grain boundary structures [14], alloying [15], and other approaches. However, the majority of advanced catalysts have shown a greater propensity for ethylene production rather than the production of liquid  $C_{2+}$  products [16–19]. For copper-based catalysts, many works focused on crystalline copper materials, and there are relatively fewer reports on amorphous copper electrocatalysts. This disparity may be attributed to the metastable structure, which will result in its unstable performance during the application. Catalysts with amorphous structures and long-range unordered atomic arrangements often possess a huge amount of surface low-coordination atoms, which always act as highly active centers for catalytic reactions. This suggests that amorphous copper is a promising candidate as an efficient electrocatalyst in electrolytic reactions, including COER [20]. Efforts to achieve efficient amorphous copper-based catalysts require precise control and stabilization of atoms and microstructures during synthesis. However, many of the existing synthesis methods, such as jet molding, laser electrodeposition, arc melting of pure metals, and mechanical alloying, etc., do not sufficiently address these considerations [21]. The catalysts synthesized by the methods mentioned typically exhibit a morphology with a large volume and small specific surface area, which may not be conducive to COER [22]. Moreover, some of these approaches require costly equipment and are often time-consuming processes, which can limit their practical applications in producing efficient and stable copper catalysts for COER [21]. Indeed, developing new approaches for creating stable amorphous copper-based catalysts with the potential for size and structure optimization is crucial for advancing their application in COER.  $SiO_2$  is a widely used carrier for various heterogeneous catalysts due to its properties, such as abundant content, low cost, and high specific surface area. The interface between copper (Cu) species and silica can increase the strength of the Cu-O bond, thereby increasing the recombination resistance of Cu species and

obtaining a catalyst with good stability [23]. Therefore, a catalyst combining Cu species with SiO<sub>2</sub> can be designed for COER application. One potential approach is leveraging electrostatic interactions, which involve the attraction between species with opposite charges, such as cations and anions. This concept provides a promising basis for the fixation of metal ions and atoms to achieve amorphization in copper catalysts [24,25].

In the present work, catalysts based on amorphous spherical copper, denoted as CuO@C-SiO<sub>2</sub>-X (where X is calcination temperatures of 400 °C, 500 °C, 600 °C, 700 °C, and 800 °C), were prepared via an electrostatic interaction process, followed by an in-situ hydrothermal treatment method [26]. The electrochemical results showed that the CuO@C-SiO<sub>2</sub>-500 electrocatalyst had the highest selectivity in COER to C<sub>2+</sub> products, especially liquid C<sub>2+</sub> products, including ethanol and acetic acid. The presence of carbon in SiO<sub>2</sub> could improve the electronic conductivity and electrochemical properties. Besides that, the catalyst possessed good stability during the long-term study. Through characterization and electrochemical performance tests, the catalyst morphology properties and catalytic efficiency of the CuO@C-SiO<sub>2</sub>-X material were revealed, and the electrochemical properties were further demonstrated. Trace amounts of carbon in the material could enhanced its electrochemical properties, and the silica not only could protect the amorphous CuO from aggregation into the crystal state but also provide a mesoporous structure for gas molecule diffusion and mass transfer. The present work not only offers a strategy for CO electroreduction to C<sub>2+</sub> liquid products but also provides a feasible way for the construction of amorphous materials with abundant active sites. The findings are also expected to offer an important reference in the formation of C<sub>2+</sub> liquid products in COER.

## 2. Materials and methods

### 2.1. Preparation of CuO@C-SiO<sub>2</sub>-X

CuO@C-SiO<sub>2</sub>-X catalysts were synthesized using the solvothermal method, as modified from a previous study [27]. The synthesis began with the dissolution of 0.25 mol of CuCl<sub>2</sub> in 10 mL of deionized water under stirring. Tetraethyl orthosilicate (3 mL) was then added to the CuCl<sub>2</sub> solution with continued stirring. After that, ammonia (1 mL) was introduced under stirring for an additional 30 min. This mixture was promptly transferred to a 50mL Teflon-lined stainless-steel autoclave and was heated at 100 °C for 12 h. Upon cooling to ambient temperature, the solution underwent centrifugation at 6000 rpm, followed by washing with water several times. After that, the drying process took place under a vacuum condition at 80 °C for 12 h. Then, the catalyst was placed in a ceramic boat and calcined at 500 °C for 3 h at a heating rate of 5 °C/min in an air atmosphere. The synthesized catalyst was denoted as CuO@C-SiO<sub>2</sub>-500. The carbon in the catalyst was kept during the heat treatment for protection by SiO<sub>2</sub> to avoid combustion. In this aspect, the CuO@C-SiO<sub>2</sub>-500 catalyst possessed a carbon content of 0.96%. Even in the CuO@C-SiO<sub>2</sub>-800 catalyst, the carbon content was tested to be 0.338% by using a total organic carbon analyzer (TOC, TOC-V CPH, Shimadzu).

For comparison, the CuO@C-SiO<sub>2</sub> material was subjected to heat treatment at different temperatures, resulting in the formation of CuO@C-SiO<sub>2</sub>-400, CuO@C-SiO<sub>2</sub>-600, CuO@C-SiO<sub>2</sub>-700, and CuO@C-SiO<sub>2</sub>-800. Additionally, to examine the impact of different copper precursors on the reaction, CuCl<sub>2</sub> was replaced by CuBr<sub>2</sub>, CuI, Cu(NO<sub>3</sub>)<sub>2</sub>, and Cu(OAc)<sub>2</sub>, where these catalysts were denoted as CuO@C-SiO<sub>2</sub>-Br, CuO@C-SiO<sub>2</sub>-I, CuO@C-SiO<sub>2</sub>-NO<sub>3</sub>, and CuO@C-SiO<sub>2</sub>-OAc, respectively. In addition, in order to exclude the effect of the carbon-silicon material, we heated and stirred the CuO@C-SiO<sub>2</sub>-500 catalyst with a higher concentration of sulfuric acid for 6 h in order to remove the CuO, followed by cooling, washing with water to neutral, and drying to obtain C-SiO<sub>2</sub>.

## 2.2. Materials

Copper chloride dihydrate (Macklin, 99.95%), tetraethyl silicate (Macklin, 98%), potassium hydroxide (Macklin, 95%), ammonia (Damao, 25%), Nafion (perfluorinated Nafion resin with a mixture of short-chain fatty alcohols and water as a solvent at a concentration of 5 wt%, of which 45% was water), and a carbon fiber paper carrier (YLS-30T) were purchased from commercial resources. Carbon monoxide (99.99%) was obtained from Xi'an Teda Cryogenic Equipment Co., Ltd. Other reagents and chemicals were purchased from commercial sources. All chemicals were used directly without further purification.

## 2.3. Catalyst characterization

X-ray diffraction (XRD) patterns were acquired using Rigaku D/Max 2500, which employed nickel-filtered copper K $\alpha$  radiation ( $\lambda = 0.154$  nm) at 40 kV and 20 mA, with a scanning rate of 10°/min. Transmission electron microscopy (TEM) images of the samples were obtained using a Talos F200x (Tecnai G2 F20) microscope. X-ray photoelectron spectroscopy (XPS) spectra were procured using a K-Alpha XPS spectrometer (Thermo Fisher Scientific), which exploited Al K $\alpha$  as the source of excitation ( $h\nu = 1486.6$  eV) and functioned at 15 kV and 20 mA. N<sub>2</sub> adsorption/desorption isotherms were recorded by using an ASAP 2460 (Micromeritics, USA) analyzer. The specific surface areas of the catalysts were ascertained through the Brunauer-Emmett-Teller (BET) method. The total pore volume was computed by employing the single-point adsorption method at P/P<sub>0</sub> = 0.99, and the average pore size was determined by using the Barrett-Joyner-Halenda method.

## 2.4. Electrode preparation

Three milligrams of the catalyst were dispersed in a mixture of 600  $\mu$ L of isopropanol and 45  $\mu$ L of Nafion (5 wt%) for 1 h at room temperature. Subsequently, this well-mixed solution was applied onto a carbon fiber paper substrate (1 cm  $\times$  1 cm) and dried under light irradiation for future use.

## 2.5. CO electrochemical reduction

COER was performed in an H-type cell, which consisted of a three-electrode system of a working electrode with the CuO@C-SiO<sub>2</sub>-X catalyst, an Ag/AgCl

reference electrode, and a counter electrode (Pt mesh electrode). The electrochemical cell was separated by a Nafion-117 proton membrane into anode and cathode chambers. Initially, CO was bubbled in an electrolyte solution ( $0.1\text{ mol}\cdot\text{L}^{-1}$  KOH) for at least 30 minutes until saturated. Following that, the catalyst was in-situ activated, which was determined via linear scanning voltammetry. For COER testing, the product was collected after every 1 h of reaction. In all measurements, the potential (relative to Ag/AgCl) was converted into RHE using the following formula:

$$E_{\text{vs. RHE}} = E_{\text{vs. Ag/AgCl}} + 0.197 + 0.059 \times \text{pH}$$

The gas product was analyzed using a GC-9790II gas chromatograph (Zhejiang Fuli Analytical Instruments Co., Ltd). Alkanes and olefins were analyzed using a flame ionization detector and  $\text{H}_2$  was analyzed using a thermal conductivity detector. The liquid product was quantified using a Bruker AVIII 600 MHz NMR spectrometer.

### 3. Results and discussion

The  $\text{CuO}@C\text{-SiO}_2\text{-X}$  catalysts created were extensively characterized using advanced technologies. **Figure A1** presents the scanning electron microscopy (SEM) images of the  $\text{CuO}@C\text{-SiO}_2\text{-X}$  catalysts, which shows that the  $\text{CuO}@C\text{-SiO}_2\text{-500}$  material behaved as a particle with sparse branching at the tip. From the transmission electron microscopy images (TEM),  $\text{CuO}@C\text{-SiO}_2\text{-500}$  consisted of spherical particles with fine branches on the surface, as shown in **Figure 1(a)** and **1(b)**. This observation was consistent with that of the findings from the SEM images. The branches of the catalyst were the crystal whiskers of the material. The presence of these branches was important for the reaction, since they contained the active sites, especially the CuO and carbon components, for the reaction. Besides that, these branches can increase the contact probability between the active sites with CO and water, and this was very important for the material, especially with a low BET specific surface area. In an electrocatalysis process, such a rough surface can promote the establishment of a localized electrochemical microenvironment [26]. From the SEM mapping, the main component for these branches was the same as the bulk structure of  $\text{CuO}@C\text{-SiO}_2\text{-500}$ . The high-resolution TEM (HRTEM) image (**Figure 1(c)**) clearly shows the contour between the spherical body and the branches, and there were no lattice fringes in this image, indicating that both copper oxide and silica were in an amorphous state, as further confirmed by the fuzzy diffraction rings in the selective region electron diffraction (SAED) image (inset in **Figure 1(b)**). Concurrently, as illustrated in **Figure 1(d–h)**, the HAADF images and corresponding EDS element mappings show the uniform distribution of C, Cu, Si, and O elements across the entire  $\text{CuO}@C\text{-SiO}_2\text{-500}$  sample with no evidence of crystal aggregation. The carbon element could be found. The energy spectrum recorded the percentages of C, Cu, Si, and O elements as 0.96%, 10.91%, 39.60%, and 48.53%, respectively (**Figure 1(i)**). The Cu loading, as tested using inductively coupled plasma-optical emission spectrometry, was 9.9% and consistent with the energy spectrum.

From the SEM images of the catalysts calcined at diverse temperatures in **Figure A1**, the samples demonstrated minor structural variations. Particularly, low-temperature-calcined catalysts exhibited denser surface burrs, whereas catalysts calcined at high temperatures resulted in comparatively sparse burrs. Combined with

the activity assessment, the results of the SEM images suggested that the number of burrs surrounding the particles could probably influence the catalytic activity. Thus, ensuring an appropriate active site exposure benefits the COER reaction.

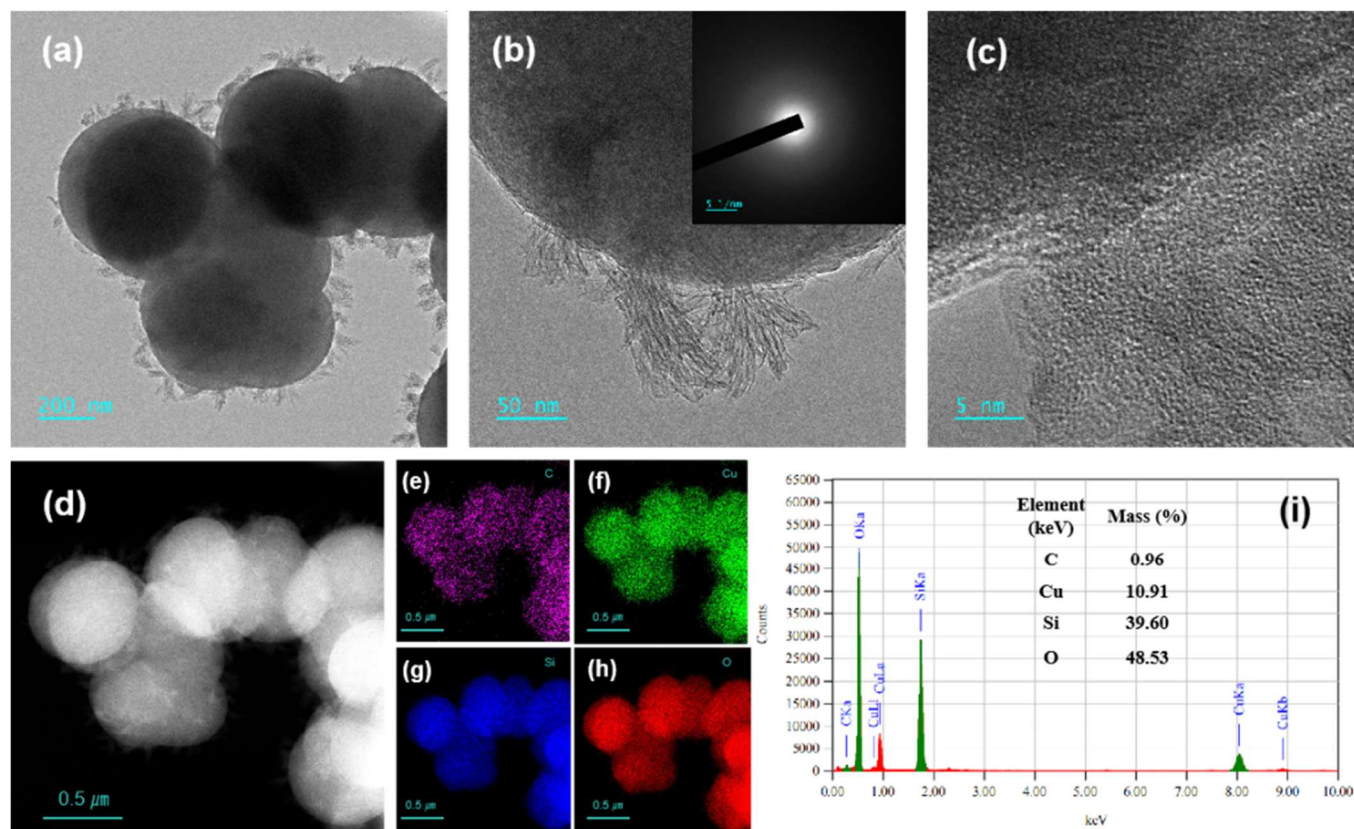


**Figure 1.** (a–b) TEM images of CuO@C-SiO<sub>2</sub>-500, where inset in (b) is SAED image. (c) HRTEM image. (d) HAADF image. (e–h) Corresponding EDS elemental mappings. (i) EDS energy spectrum of CuO@C-SiO<sub>2</sub>-500 catalyst.

The XRD profiles of the CuO@C-SiO<sub>2</sub>-X catalysts calcined at various temperatures are shown in **Figure 2(a)**. The peak at 22° in the XRD pattern was a characteristic broad peak, indicating the amorphous nature of the silica [27,28]. The CuO@C-SiO<sub>2</sub>-X catalysts calcined at 700 °C and 800 °C had a series of diffraction peaks at  $2\theta = 32.5^\circ, 35.6^\circ, 38.7^\circ, 48.7^\circ, 61.5^\circ,$  and  $66.2^\circ$  that could be classified as CuO (PDF#80-1917) [26,29]. The XRD patterns did not show any peaks assigned to CuO in the CuO@C-SiO<sub>2</sub>-X samples calcined at 400 °C–600 °C, indicating that CuO was in an amorphous form in these catalysts. From the element mappings, the Cu species were well dispersed on the whole grain, certifying that the Cu species were incorporated into the structure of SiO<sub>2</sub>. The XRD spectra of catalysts derived from different copper salt precursors are shown in **Figure 2(b)**. There was only a typical broad peak of silica at around 22°, and no other peaks were present. The result indicated the catalysts derived from different copper salt precursors had also an amorphous structure. According to **Figure A2**, we found that the amorphous form of the catalyst was enhanced after the reaction, and no peaks of SiO<sub>2</sub>, CuO, and Cu<sub>2</sub>O were observed. SiO<sub>2</sub> played an important role in the reaction, and it could prevent Cu species from aggregating into the crystal state.

The Fourier transform infrared spectroscopy (FTIR) spectra of the CuO@C-SiO<sub>2</sub>-X catalysts are given in **Figure 2(c)**. The absorption peak at 1621.8 cm<sup>-1</sup> corresponded to the expansion and contraction vibration of the C-O bond [30], further confirming the presence of the C element in the catalyst. The absorption peaks that appeared at 789.9 cm<sup>-1</sup> and 1090.5 cm<sup>-1</sup> could be assigned to the expansion and contraction vibration of the Si-O-Si bond. At 468.12 cm<sup>-1</sup>, a telescopic vibrational absorption peak of Cu-O was observed. Characterization peaks were found at 1090.5 cm<sup>-1</sup>, 789.9 cm<sup>-1</sup>, and 468.1 cm<sup>-1</sup> for the infrared absorption peaks of the CuO@C-SiO<sub>2</sub>-X materials [31,32], indicating the presence of SiO<sub>2</sub> and CuO in the catalysts [33].

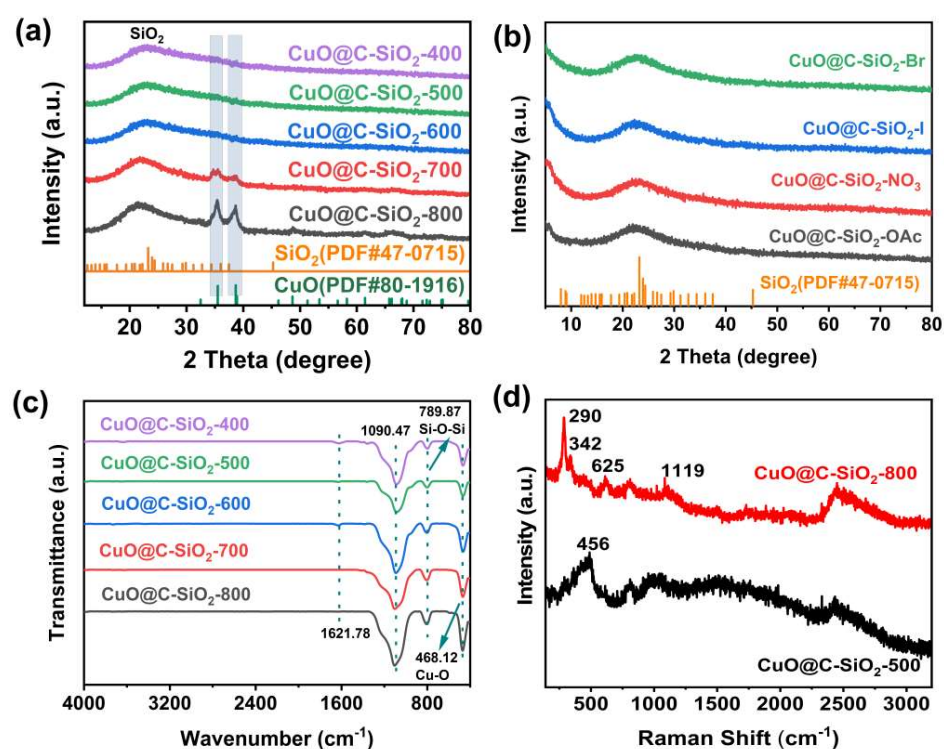


**Figure 2.** (a) XRD patterns of CuO@C-SiO<sub>2</sub>-X catalysts calcined at various temperatures, (b) XRD patterns of CuO@C-SiO<sub>2</sub>-X catalysts derived from different copper sources, (c) FT-IR of CuO@C-SiO<sub>2</sub>-X catalysts, and (d) Raman spectra of CuO@C-SiO<sub>2</sub>-500 and CuO@C-SiO<sub>2</sub>-800 catalysts.

Raman spectroscopy was performed to further verify the presence and chemical information of Cu and Si on the surface of the catalysts. Theoretically, copper oxide is a monoclinic structure with the symmetry of the  $C_{2h}^6$  space group [34,35]. According to the space group theory, copper oxide has 12 central photo phonon modes,  $\Gamma = 4A_u + 5B_u + A_g + 2B_g$ . Among them, ( $A_u + 2B_u$ ) are acoustic modes, ( $A_u + 3B_u$ ) are infrared active modes, and ( $A_g + 2B_g$ ) are Raman active modes [34,35]. As seen in **Figure 2(d)**, the CuO@C-SiO<sub>2</sub>-500 and the CuO@C-SiO<sub>2</sub>-800 had completely different Raman peaks. The former has a distinct Raman peak at 456 cm<sup>-1</sup>, assigned to the bending vibration of the O-Si bond. However, the CuO@C-SiO<sub>2</sub>-800 had three peaks at 290 cm<sup>-1</sup>, 342 cm<sup>-1</sup>, and 625 cm<sup>-1</sup>, assigned to the  $A_g$ ,  $B_g^1$ , and  $B_g^2$  modes

of CuO crystals, respectively [36–38], indicating the presence of large copper oxide structures in the CuO@C-SiO<sub>2</sub>-800 sample. Based on the Raman peak at 1119 cm<sup>-1</sup>, it was inferred that the interaction between CuO and SiO<sub>2</sub> and the crystal defects led to the occurrence of non-Raman active vibrations. The peaks contributed to CuO were not found in the CuO@C-SiO<sub>2</sub>-500 catalyst, suggesting that the Cu species were different from those in the CuO@C-SiO<sub>2</sub>-800 catalyst. This result was in agreement with the results in XRD and FT-IR described above.

XPS was used to ascertain the surface composition and chemical states in the CuO@C-SiO<sub>2</sub>-X samples. **Figure 3** presents the analyzed surface constituents of the CuO@C-SiO<sub>2</sub>-500 and the CuO@C-SiO<sub>2</sub>-800 samples. By examining the Cu 2p spectrum of the CuO@C-SiO<sub>2</sub>-500 sample, we observed a peak at 934.6 eV, which was ascribed to the Cu<sup>2+</sup> 2p<sub>3/2</sub> state, and another peak at 954.4 eV, which corresponded to the Cu<sup>2+</sup> 2p<sub>1/2</sub> state [39–41]. A comparison between the Cu 2p XPS spectra of CuO@C-SiO<sub>2</sub>-500 and CuO@C-SiO<sub>2</sub>-800 (**Figure 3(a)** and **3(d)**) did not show a remarkable difference, confirming that the varied activities were not derived from the chemical valance of samples calcined at diverse temperatures. As seen from **Figure 3(b)** and **3(e)**, the O 1s XPS spectra could be fitted into three peaks at 533.2 eV, 532.5 eV, and 531.5 eV, attributing to Si-OH, Si-O, and O=Cu, respectively. The Si 2p spectra, as depicted in **Figure 3(c)** and **3(f)**, showcased a singleton peak at 103.1 eV, which was indicative of the existence of silica in the catalysts [42]. The XPS results confirmed that the different catalytic activities between the CuO@C-SiO<sub>2</sub>-500 and the CuO@C-SiO<sub>2</sub>-800 samples did not stem from the chemical valance compositions.

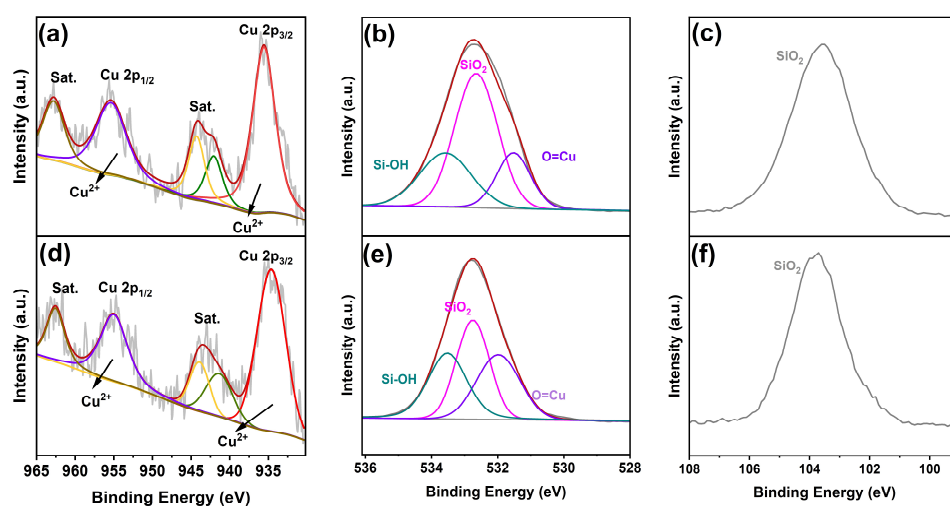


**Figure 3.** XPS spectra of (a) CuO@C-SiO<sub>2</sub>-500 Cu 2p, (b) CuO@C-SiO<sub>2</sub>-500 O 1s, (c) CuO@C-SiO<sub>2</sub>-500 Si 2p, (d) CuO@C-SiO<sub>2</sub>-800 Cu 2p, (e) CuO@C-SiO<sub>2</sub>-800 O 1s, and (f) CuO@C-SiO<sub>2</sub>-800 Si 2p.

As illustrated in **Figure A3**, we conducted the N<sub>2</sub> adsorption/desorption isotherms to study the textural properties of the prepared samples. Based on the gathered isotherms, we determined the pore size distributions and specific surface areas of the catalysts, as detailed in **Table A1**. Following the International Union of Pure and Applied Chemistry (IUPAC) criteria, each tested catalyst demonstrated a Type IV isotherm character and an H3-type hysteresis loop. This pattern suggested the

presence of mesoporous structures in all examined samples. Different calcination temperatures resulted in varying BET surface areas and pore sizes across the catalysts. Specifically, the BET surface areas were as follows:  $31 \text{ m}^2 \cdot \text{g}^{-1}$  for the catalyst calcined at  $400 \text{ }^\circ\text{C}$ ,  $28 \text{ m}^2 \cdot \text{g}^{-1}$  for catalysts calcined at  $500 \text{ }^\circ\text{C}$  and  $600 \text{ }^\circ\text{C}$ ,  $45 \text{ m}^2 \cdot \text{g}^{-1}$  for the catalyst calcined at  $700 \text{ }^\circ\text{C}$ , and  $35 \text{ m}^2 \cdot \text{g}^{-1}$  for the catalyst calcined at  $800 \text{ }^\circ\text{C}$ . Out of the tested catalysts, the  $\text{CuO}@C\text{-SiO}_2\text{-500}$  sample demonstrated the smallest specific surface area. However, subsequent evaluations of the COER revealed its superior performance in catalytic reactions, which implied that the specific textural structure of this sample did not affect its catalytic efficiency and that mass transfer and diffusion were not the rate-determining steps for the COER reaction.

#### 4. Catalytic performances of electrochemical CO reduction

To conduct an evaluation of the COER performances of the  $\text{CuO}@C\text{-SiO}_2\text{-X}$  samples, linear sweep voltammetry (LSV) profiles were recorded in a CO-saturated KOH ( $0.1 \text{ mol} \cdot \text{L}^{-1}$ ) solution, with a scan rate fixed at  $100 \text{ mV} \cdot \text{s}^{-1}$  across a potential range from  $-0.54 \text{ V}$  to  $-0.79 \text{ V}$  (vs. RHE). The LSV profiles, presented in **Figure 4(a)**, displayed the impact of different calcination temperatures on catalytic performance. Notably, the COER current density associated with these materials first increased as the calcination temperature increased, peaking at  $500 \text{ }^\circ\text{C}$ , and then decreased. The highest current density on the  $\text{CuO}@C\text{-SiO}_2\text{-500}$  catalyst was probably derived from the availability of active sites on the catalyst.

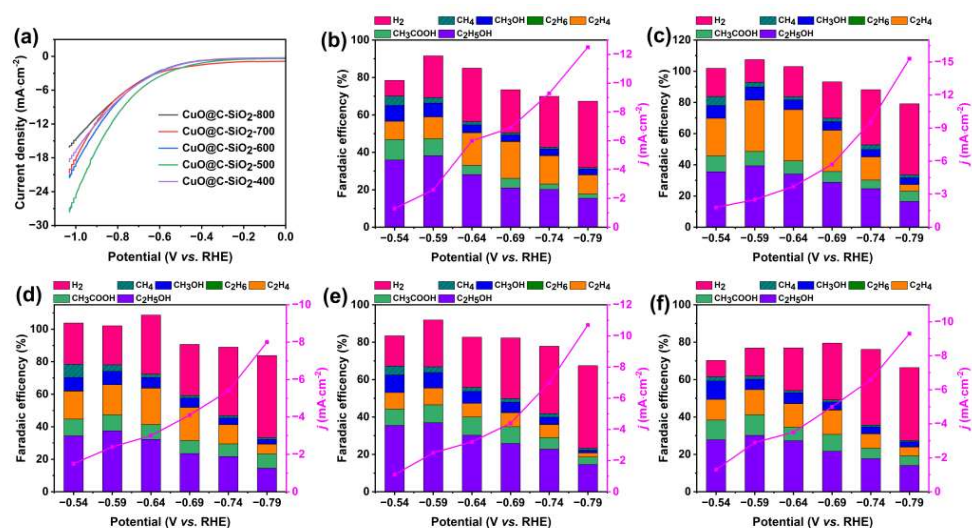


**Figure 4.** (a) LSV curves of different catalysts in CO-saturated  $0.1 \text{ mol} \cdot \text{L}^{-1}$  of KOH aqueous electrolyte. Catalytic performances of COER over (b)  $\text{CuO}@C\text{-SiO}_2\text{-400}$ , (c)  $\text{CuO}@C\text{-SiO}_2\text{-500}$ , (d)  $\text{CuO}@C\text{-SiO}_2\text{-600}$ , (e)  $\text{CuO}@C\text{-SiO}_2\text{-700}$ , and (f)  $\text{CuO}@C\text{-SiO}_2\text{-800}$ .

To further probe into how calcination temperature influences the catalytic activity, detailed COER experiments were studied by using the  $\text{CuO}@C\text{-SiO}_2\text{-X}$  catalysts. **Figures 4(b-f)** show the FE values of various electrochemical reduction products, such as H<sub>2</sub>, methane, methanol, ethane, ethylene, ethanol, etc., in the range of  $-0.54 \sim -0.79 \text{ V}$  (vs. RHE) for the  $\text{CuO}@C\text{-SiO}_2\text{-X}$  catalysts in  $0.1 \text{ mol} \cdot \text{L}^{-1}$  of KOH.

From the gas products detected by gas chromatography (GC), C<sub>2</sub>H<sub>4</sub> and H<sub>2</sub> were the main components in the gaseous product obtained from the CuO@C-SiO<sub>2</sub>-X catalyst, while ethanol was the main product in liquid, as confirmed by the hydrogen-1 nuclear magnetic resonance (<sup>1</sup>H NMR) (**Figures A4 and A5**). Remarkably, the CuO@C-SiO<sub>2</sub>-500 catalyst manifested the highest FE for C<sub>2+</sub> products (FE<sub>C<sub>2+</sub></sub>) at 81.5%, coupled with a current density reaching 2.5 mA·cm<sup>-2</sup> (**Figure 4(c)**). It is important to note, however, that the relatively low current density was derived from the low conductive nature of the doped SiO<sub>2</sub> and the FE with lower than 100% was probably due to the consumption of electric quantity caused by the reduction of the CuO@C-SiO<sub>2</sub>-500 catalyst and the heat production for the high internal resistance during the reaction. These ohmic loss and energy loss caused the reduction in total FE values. The presence of carbon could improve the conductivity of the samples. In order to exclude the effect of the carbon-silicon material on the catalytic performance of CuO@C-SiO<sub>2</sub>-X samples, we investigated the catalytic performance of the C-SiO<sub>2</sub> material in the COER reaction, which produced only 1.18% FE of methane and a negligible amount of the C<sub>2+</sub> product. The obtained GC for the reaction gas and the obtained <sup>1</sup>H NMR for the electrolyte are shown in **Figures A6 and A7**, respectively. As documented in **Table 1**, compared with reported catalysts, the CuO@C-SiO<sub>2</sub>-500 catalyst delivered the highest FE to C<sub>2+</sub> chemicals.

**Table 1.** Reported catalysts for CO reduction in aqueous electrolytes.

Catalyst	Electrolyte	Potential (V vs. RHE)	FE <sub>C<sub>2+</sub></sub> (%)	Products	J (mA·cm <sup>-2</sup> )	Cell	Ref.
Oxide-derived Cu	0.1M KOH	-0.3	57%	EtOH (~42%) Acetate (~15%)	~0.02	H-cell	[14]
Cu NPs (grain boundaries)	0.1M KOH	-0.3	~70%	EtOH (~35%) Acetate (~35%)	~0.04	H-cell	[43]
Polycrystalline Cu	0.1M KOH	-0.59	~42%	Ethylene (30%) EtOH (~12%)	1.2	H-cell	[44]
Polycrystalline Cu/PTEE	0.1M KOH	-0.94	65%	Ethylene (~35%) EtOH (~15%) Acetate (~15%) Methane (~15%)	~150	Flow cell	[18]
Cu nanosheets	2M KOH	-0.75	~70%	Ethylene (~15%) Acetate (~48%)	131	Flow cell	[13]
Cu NPs	1M KOH	-0.7	~62%	Ethylene (52.7%) EtOH (~9%)	14.9	H-cell	[45]
CuO@C-SiO <sub>2</sub> -500	0.1M KOH	-0.59	~81.5%	Ethylene (32.9%) EtOH (39.4%) Acetate (9.2%)	2.5	H-cell	This work

The effect of varying applied potentials from -0.54 V to -0.79 V (vs. RHE) on the FE<sub>C<sub>2+</sub></sub> and current density of the catalysts was also thoroughly investigated. As an example, the results for the CuO@C-SiO<sub>2</sub>-500 catalyst are shown in **Figure 4(c)**, where its FE<sub>C<sub>2+</sub></sub> initially increased and reached the highest at 81.5% at -0.59 V (vs. RHE), before decreasing with further increases in the applied potential greater than -0.64 V (vs. RHE). At lower potentials (<-0.59 V vs. RHE), the FE for liquid products surpassed those for gas products. From -0.59 V to -0.79 V, the FE<sub>C<sub>2</sub>H<sub>4</sub></sub> and FE<sub>C<sub>2</sub>H<sub>5</sub>OH</sub> values declined, but FE<sub>H<sub>2</sub></sub> increased remarkably. This transition can be attributed to the influence of the kinetic mass transfer of carbon monoxide, with the hydrogen evolution reaction becoming the dominant reaction [46].

Electrolytes are highly important in electrochemical reactions, as they facilitate the interaction between cations and anions with active sites and they adjust the interplay among reactants, intermediates, and the products from a catalyst and

electrode surfaces. A deep comprehension of an electrolyte's role could contribute significantly to enhancing catalyst activity and  $C_{2+}$  product selectivity. **Figure 5(a)** illustrates the influence of different concentrations of the KOH electrolyte on catalytic efficiency at  $-0.59$  V for the  $CuO@C-SiO_2-500$  catalyst. With the increase in KOH concentration, the  $FE_{C_{2+}}$  value showed a decreasing trend. At  $0.1 \text{ mol}\cdot\text{L}^{-1}$  of KOH,  $FE_{C_{2+}}$  achieved a peak value of 81.5%, but the total current density was the lowest for the lowest electrical conductivity. An increase in the KOH concentration led to a rise in  $FE_{H_2}$ , suggesting that a higher electrolyte concentration might impede the formation of  $C_{2+}$  species, while favoring the hydrogen evolution reaction instead.

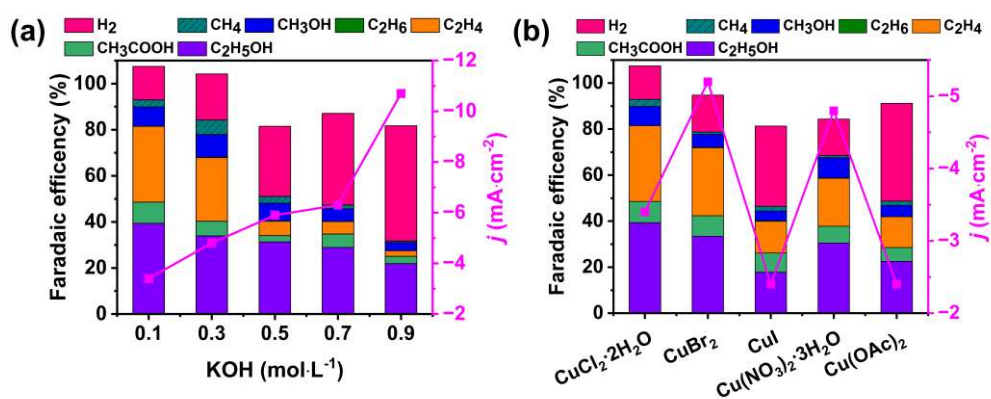


**Figure 5.** (a) Catalytic performances of COER:  $CuO@C-SiO_2-500$  catalyst at different concentrations of KOH electrolyte and (b) catalysts derived from diverse Cu salts precursors at  $-0.59$  V (vs. RHE).

A further examination of how copper salt precursors influenced COER performances was conducted by assessing the electrochemical behavior of catalysts derived from five copper salt precursors. As shown in **Figure 5(b)**, the use of  $CuCl_2$  yielded the highest  $FE_{C_{2+}}$ . A plausible explanation for this phenomenon is the presence of trace amounts of  $Cl^-$  ions within the catalyst, which likely promoted the generation of  $C_{2+}$  species during the reaction. Previous studies confirmed that  $Cl^-$  can enhance the adsorption of  $^*CO$  on the surface of a catalyst and reduce the energy barrier of the C-C coupling, further promoting the formation of multi-carbon ( $C_{2+}$ ) products [47–49].

The electrochemically active surface area (ECSA) was determined by conducting double-layer capacitance tests, as illustrated in **Figure A8**. Cyclic voltammetry scans were conducted from  $0.668$  V to  $0.861$  V (vs. RHE) at various scan rates of 60, 80, 100, 120, and  $140 \text{ mV}\cdot\text{s}^{-1}$ . **Figure 6(a)** demonstrates the relationship between the scan rate and the change in current density ( $\Delta j = j_a - j_c$ , where  $j_a$  and  $j_c$  represent the anodic and cathodic current densities, respectively). The result of **Figure 6(a)** was obtained from **Figure A8**, i.e., the fitted slopes of the ECSA for each catalyst. Among the tested samples, the  $CuO@C-SiO_2-500$  catalyst exhibited the highest slope of  $0.98 \text{ mF}\cdot\text{cm}^{-2}$  at a potential of  $-0.6$  V (vs. RHE) in  $0.1 \text{ mol}\cdot\text{L}^{-1}$  of KOH, indicating the largest electrochemically active area and the potential for a superior COER activity. Notably, there was a small discrepancy in the ECSA and the COER performance of  $CuO@C-SiO_2-400$  ( $0.92 \text{ mF}\cdot\text{cm}^{-2}$ ),  $CuO@C-SiO_2-500$  ( $0.98 \text{ mF}\cdot\text{cm}^{-2}$ ),  $CuO@C-SiO_2-600$  ( $0.96 \text{ mF}\cdot\text{cm}^{-2}$ ), and  $CuO@C-SiO_2-700$  ( $0.95 \text{ mF}\cdot\text{cm}^{-2}$ ). However, the ECSA value

for the CuO@C-SiO<sub>2</sub>-800 catalyst was significantly lower at 0.67 mF·cm<sup>-2</sup>, which was attributed to its better crystallinity and fewer active sites. The aforementioned data suggested that the CuO@C-SiO<sub>2</sub>-500 catalyst, with its amorphous CuO, promoted the COER activity compared with other catalysts subjected to various calcination temperatures. The hybrid carbon could enhance the electrical conductivity of the catalyst. Additionally, the interfacial reaction kinetics were probed for the catalysts calcined at diverse temperatures via their Tafel slopes, with the findings presented in **Figure 6(b)**. A smaller Tafel slope signifies a reduced kinetic energy demand for the CO activation. Consistent with the ECSA result, the CuO@C-SiO<sub>2</sub>-500 catalyst displayed the lowest Tafel slope at 43.29 mV·dec<sup>-1</sup>, while the CuO@C-SiO<sub>2</sub>-800 possessed the highest at 53.50 mV·dec<sup>-1</sup>. These findings confirmed that the CuO@C-SiO<sub>2</sub>-500 catalyst, with its amorphous CuO species, considerably diminished the kinetic energy barrier, favorably impacting the reaction kinetics.

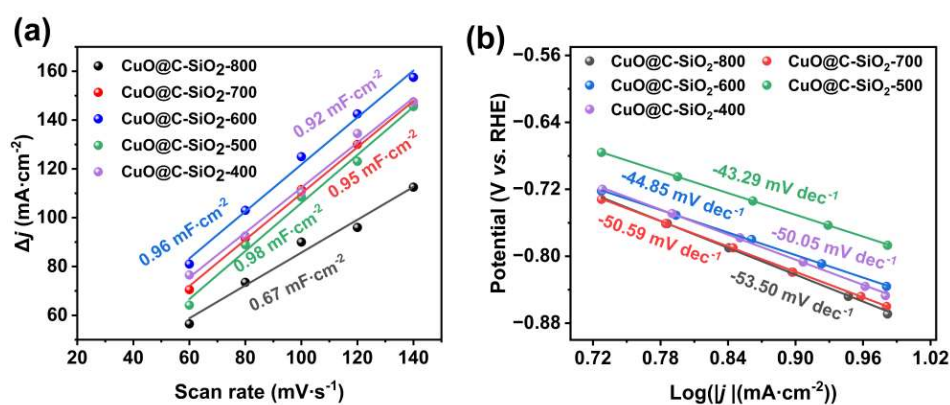


**Figure 6.** CuO@C-SiO<sub>2</sub>-X catalysts: **(a)** electrochemically active surface area (ECSA) and **(b)** Tafel slopes.

The kinetics of charge transfer for the catalysts during the COER reaction were probed by conducting electrochemical impedance spectroscopy (EIS) measurements in 0.1 mol·L<sup>-1</sup> of KOH. These measurements were obtained by setting the AC perturbation voltage amplitude at 5 mV, with the frequency of scans spanning from 0.01 Hz to 100 kHz. The study of charge transfer is primarily linked to the high-frequency range, which is indicative of an electrode's reaction dynamics. The high-frequency semicircular arc represents the charge transfer resistance ( $R_{ct}$ ), while the low-frequency regime is attributed to the diffusion of reactants or products. The smaller the diameter of the resulting curve, the lower the material resistance and the better the charge transfer. As illustrated in **Figure 7(a)**, among the catalysts subjected to different calcination temperatures, the CuO@C-SiO<sub>2</sub>-500 catalyst exhibited the lowest electrode impedance, confirming the findings from prior LSV analyses. Combined with the results of the ECSA test, the CuO@C-SiO<sub>2</sub>-500 catalyst had the highest current density and ECSA values, leading to the inference that it had superior catalytic performance and the highest electrochemical activity.

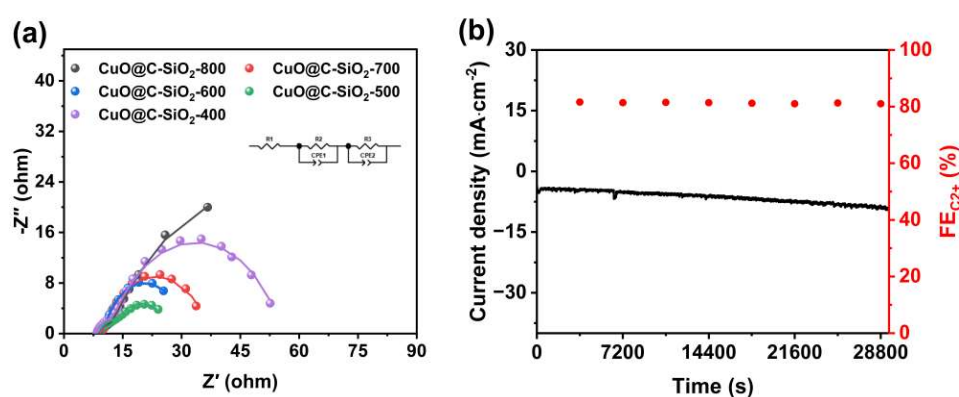


**Figure 7.** (a) Electrochemical impedance spectroscopy (EIS) of catalysts calcined at different temperatures in  $0.1 \text{ mol}\cdot\text{L}^{-1}$  of KOH electrolyte and (b) stability of  $\text{CuO}@C\text{-SiO}_2\text{-500}$  catalyst at  $-0.59 \text{ V}$  (vs. RHE) in  $0.1 \text{ mol}\cdot\text{L}^{-1}$  of KOH electrolyte.

Under an optimal condition, the stability of the  $\text{CuO}@C\text{-SiO}_2\text{-500}$  catalyst was evaluated in a long-term stability test for approximately 8 h (**Figure 7(b)**). As the reaction proceeded, the  $\text{FE}_{\text{C}_2+}$  and the current density exceeded  $80\%$  and  $2.5 \text{ mA}\cdot\text{cm}^{-2}$ , respectively. However, both these values gradually changed over time at an acceptable level. The loss in  $\text{FE}_{\text{C}_2+}$  and the increase in current density for the liquid  $\text{C}_2+$  product may be ascribable to the electrolyte pH change close to the local electrode and variation of the Cu valance state.

XPS analysis was performed on the reacted catalyst, as shown in **Figure A9**. The results revealed the presence of  $\text{Cu}^{+0}$  in the  $\text{CuO}@C\text{-SiO}_2\text{-500}$  catalyst, denoting the partial reduction of  $\text{Cu}^{2+}$  to  $\text{Cu}^{+0}$  (**Figure A9(a)**), and this was further confirmed by the Cu LMM spectrum (**Figure A9(d)**). The Cu LMM spectrum indicated the presence of  $\text{Cu}^+$ . The  $\text{CuO}@C\text{-SiO}_2\text{-500}$  Si 2p and O 1s spectra were unchanged compared with those of the fresh samples (**Figure A9(b)** and **9(c)**), suggesting that there was no significant change in the valence of Si and O after the catalyst was used. In conjunction with the SEM image of the used  $\text{CuO}@C\text{-SiO}_2\text{-500}$  catalyst (**Figure A10**), it was apparent that the overall morphology of the catalyst remained the spherical structure compared with those of the fresh catalysts. However, the  $\text{CuO}@C\text{-SiO}_2\text{-500}$  catalyst showed no branched tips, which was because of the flushing of the electrolyte. Thus, these branches were lost during the long-term reaction, and this was one of the main reasons for the loss of activity for the reaction. The result indicated that the  $\text{CuO}@C\text{-SiO}_2\text{-500}$  catalyst possessed acceptable stability during the reaction.

## 5. Conclusion

In summary, we fabricated a series of amorphous  $\text{CuO}@C\text{-SiO}_2\text{-X}$  catalysts through a combination of electrostatic assembly and a hydrothermal approach for COER. The findings indicated that the  $\text{CuO}@C\text{-SiO}_2\text{-500}$  catalyst exhibited outstanding electrocatalytic performance and robust stability for COER, achieving the highest Faradaic efficiency of  $81.5\%$  at  $-0.59 \text{ V}$  (vs. RHE) for the  $\text{C}_2+$  products. The structural characterization and catalytic activity assessments discovered the relationship between structural properties and catalytic performances. Especially, we found that the different crystalline structures derived from diverse calcination

temperatures had a great influence on catalytic performance. Kinetic studies and electrochemical property studies showed that the CuO@C-SiO<sub>2</sub>-500 catalyst outperformed the control samples, partially due to the presence of appropriate amounts of carbon and amorphous copper oxide.

**Author contributions:** Conceptualization, ZHH, YT, JL and WW; methodology, ZHH, HHC and JL; software, YCS; data analysis, WW and HW; formal analysis, YT; investigation, ZHH and HHC; data curation, YXY; writing—original draft preparation, YXY and ZHH; writing—review and editing, ZHH and ZTL; visualization, YY; supervision, ZHH and ZTL; funding acquisition, ZTL and ZHH. All authors have read and agreed to the published version of the manuscript.

**Funding:** The authors gratefully acknowledge the financial support from the National Natural Science Foundation of China (22078182 and 22278261) and the Key Project of the Education Department of Shaanxi Province (21JY005).

**Conflict of interest:** The authors declare that they have no known competing financial interests or personal relationships that could have appeared to influence the work reported in this paper.

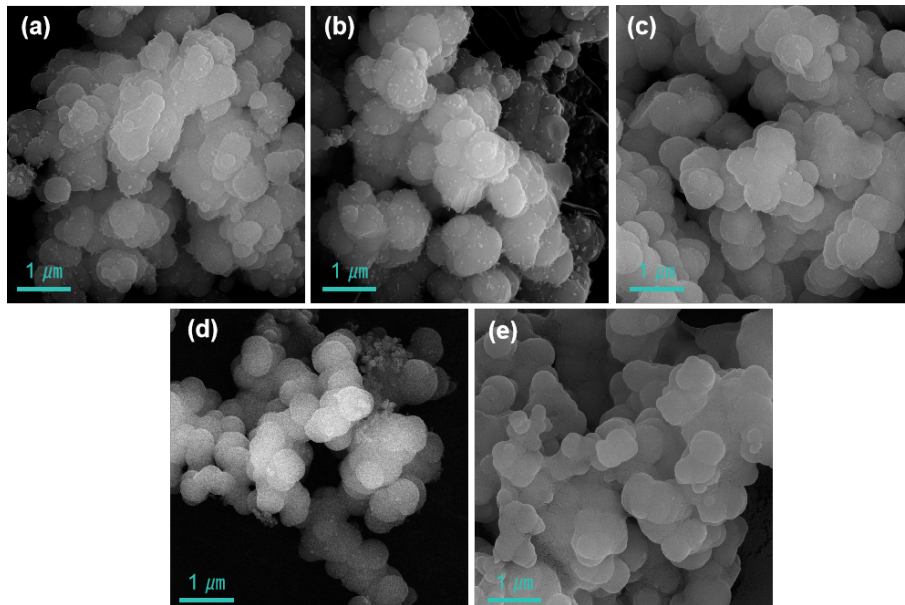
## References

1. Nitopi S, Bertheussen E, Scott SB, et al. Progress and perspectives of electrochemical CO<sub>2</sub> reduction on copper in aqueous electrolyte. *Chemical Reviews*. 2019; 119(12): 7610-7672. doi: 10.1021/acs.chemrev.8b00705
2. Zhu P, Wang H. High-purity and high-concentration liquid fuels through CO<sub>2</sub> electroreduction. *Nature Catalysis*. 2021; 4(11): 943-951. doi: 10.1038/s41929-021-00694-y
3. Chen X, Chen J, Alghoraibi NM, et al. Electrochemical CO<sub>2</sub>-to-ethylene conversion on polyamine-incorporated Cu electrodes. *Nature Catalysis*. 2020; 4(1): 20-27. doi: 10.1038/s41929-020-00547-0
4. Li J, Ozden A, Wan M, et al. Silica-copper catalyst interfaces enable carbon-carbon coupling towards ethylene electrosynthesis. *Nature Communications*. 2021; 12(1): 2808. doi: 10.1038/s41467-021-23023-0
5. Rabinowitz JA, Kanan MW. The future of low-temperature carbon dioxide electrolysis depends on solving one basic problem. *Nature Communications*. 2020; 11(1): 5231. doi: 10.1038/s41467-020-19135-8
6. Niu ZZ, Chi LP, Liu R, et al. Rigorous assessment of CO<sub>2</sub> electroreduction products in a flow cell. *Energy & Environmental Science*. 2021; 14(8): 4169-4176. doi: 10.1039/d1ee01664d
7. Li Y, Hu Y, Wu XF. Non-noble metal-catalysed carbonylative transformations. *Chemical Society Reviews*. 2018; 47(1): 172-194. doi: 10.1039/c7cs00529f
8. Guo S, Liu Y, Huang Y, et al. Promoting electrolysis of carbon monoxide toward acetate and 1-propanol in flow electrolyzer. *ACS Energy Letters*. 2023; 8(2): 935-942. doi: 10.1021/acscenergylett.2c02502
9. Wang L, Nitopi S, Wong AB, et al. Electrochemically converting carbon monoxide to liquid fuels by directing selectivity with electrode surface area. *Nature Catalysis*. 2019; 2(8): 702-708. doi: 10.1038/s41929-019-0301-z
10. Zhu P, Xia C, Liu CY, et al. Direct and continuous generation of pure acetic acid solutions via electrocatalytic carbon monoxide reduction. *Proceedings of the National Academy of Sciences*. 2020; 118(2): e2010868118. doi: 10.1073/pnas.2010868118
11. Chen C, Yan X, Liu S, et al. Highly efficient electroreduction of CO<sub>2</sub> to C<sub>2+</sub> alcohols on heterogeneous dual active sites. *Angewandte Chemie International Edition*. 2020; 59(38): 16459-16464. doi: 10.1002/anie.202006847
12. Jouny M, Luc W, Jiao F. General techno-economic analysis of CO<sub>2</sub> electrolysis systems. *Industrial & Engineering Chemistry Research*. 2018; 57(6): 2165-2177. doi: 10.1021/acs.iecr.7b03514
13. Luc W, Fu X, Shi J, et al. Two-dimensional copper nanosheets for electrochemical reduction of carbon monoxide to acetate. *Nature Catalysis*. 2019; 2(5): 423-430. doi: 10.1038/s41929-019-0269-8

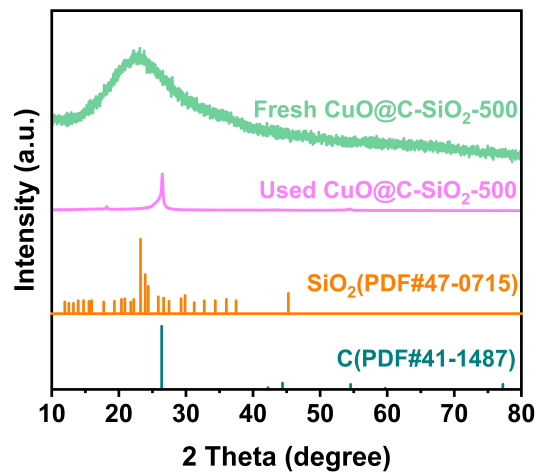
14. Li CW, Ciston J, Kanan MW. Electroreduction of carbon monoxide to liquid fuel on oxide-derived nanocrystalline copper. *Nature*. 2014; 508(7497): 504-507. doi: 10.1038/nature13249
15. Yang C, Ko BH, Hwang S, et al. Overcoming immiscibility toward bimetallic catalyst library. *Science Advances*. 2020; 6(17): eaaz6844. doi: 10.1126/sciadv.aaz6844
16. Ripatti DS, Veltman TR, Kanan MW. Carbon monoxide gas diffusion electrolysis that produces concentrated C<sub>2</sub> products with high single-pass conversion. *Joule*. 2019; 3(10): 2581. doi: 10.1016/j.joule.2019.09.012
17. Jouny M, Luc W, Jiao F. High-rate electroreduction of carbon monoxide to multi-carbon products. *Nature Catalysis*. 2018; 1(10): 748-755. doi: 10.1038/s41929-018-0133-2
18. Li J, Chang K, Zhang H, et al. Effectively increased efficiency for electroreduction of carbon monoxide using supported polycrystalline copper powder electrocatalysts. *ACS Catalysis*. 2019; 9(6): 4709-4718. doi: 10.1021/acscatal.9b00099
19. Zhao C, Luo G, Liu X, et al. In situ topotactic transformation of an interstitial alloy for CO electroreduction. *Advanced Materials*. 2020; 32(39): 2002382. doi: 10.1002/adma.202002382
20. Wang L, Higgins DC, Ji Y, et al. Selective reduction of CO to acetaldehyde with CuAg electrocatalysts. *Proceedings of the National Academy of Sciences*. 2020; 117(23): 12572-12575. doi: 10.1073/pnas.1821683117
21. Peng HJ, Tang MT, Halldin Stenlid J, et al. Trends in oxygenate/hydrocarbon selectivity for electrochemical CO<sub>2</sub> reduction to C<sub>2</sub> products. *Nature Communications*. 2022; 13(1): 1399. doi: 10.1038/s41467-022-29140-8
22. Wang X, Wang Z, Zhuang TT, et al. Efficient upgrading of CO to C<sub>3</sub> fuel using asymmetric C-C coupling active sites. *Nature Communications*. 2019; 10(1): 5186. doi: 10.1038/s41467-019-13190-6
23. Tan X, Sun K, Zhuang Z, et al. Stabilizing copper by a reconstruction-resistant atomic Cu–O–Si interface for electrochemical CO<sub>2</sub> reduction. *Journal of the American Chemical Society*. 2023, 145(15): 8656-8664. doi: 10.1021/jacs.3c01638
24. Herzog A, Bergmann A, Jeon HS, et al. Operando investigation of Ag-decorated Cu<sub>2</sub>O nanocube catalysts with enhanced CO<sub>2</sub> electroreduction toward liquid products. *Angewandte Chemie International Edition*. 2021; 60(13): 7426-7435. doi: 10.1002/anie.202017070
25. Hoang TTH, Verma S, Ma S, et al. Nanoporous copper–silver alloys by additive-controlled electrodeposition for the selective electroreduction of CO<sub>2</sub> to ethylene and ethanol. *Journal of the American Chemical Society*. 2018; 140(17): 5791-5797. doi: 10.1021/jacs.8b01868
26. Yang R, Zeng Z, Peng Z, et al. Amorphous urchin-like copper@nanosilica hybrid for efficient CO<sub>2</sub> electroreduction to C<sub>2+</sub> products. *Journal of Energy Chemistry*. 2021; 61: 290-296. doi: 10.1016/j.jechem.2020.12.032
27. Dubey RS, Rajesh YBRD, More MA. Synthesis and characterization of SiO<sub>2</sub> nanoparticles via sol-gel method for industrial applications. *Materials Today: Proceedings*. 2015; 2(4-5): 3575-3579. doi: 10.1016/j.matpr.2015.07.098
28. Nallathambi G, Ramachandran T, Rajendran V, et al. Effect of silica nanoparticles and BTCA on physical properties of cotton fabrics. *Materials Research*. 2011; 14(4): 552-559. doi: 10.1590/s1516-14392011005000086
29. Yin H, Yu XX, Li QW, et al. Hollow porous CuO/C composite microcubes derived from metal-organic framework templates for highly reversible lithium-ion batteries. *Journal of Alloys and Compounds*. 2017; 706: 97-102. doi: 10.1016/j.jallcom.2017.02.215
30. Ge Y, Shah ZH, Wang C, et al. In situ encapsulation of ultrasmall CuO quantum dots with controlled band-gap and reversible thermochromism. *ACS Applied Materials & Interfaces*. 2015; 7(48): 26437-26444. doi: 10.1021/acsami.5b09578
31. Rahimabadi Z, Bagheri-Mohagheghi MM, Shirpay A. Synthesis, characterization, and the study of structural and optical properties of core/shell nanoparticles of SiO<sub>2</sub>@CuO for solar absorption collectors application. *Journal of Materials Science: Materials in Electronics*. 2022; 33(10): 7765-7780. doi: 10.1007/s10854-022-07928-0
32. Prakash J, Shekhar H, Yadav SR, et al. Synthesis and characterization of plant derived copper oxide nanoparticles and their application towards oxygen reduction reaction. *ChemistrySelect*. 2022; 7(1): e202103594. doi: 10.1002/slct.202103594
33. Ding J, Popa T, Tang J, et al. Highly selective and stable Cu/SiO<sub>2</sub> catalysts prepared with a green method for hydrogenation of diethyl oxalate into ethylene glycol. *Applied Catalysis B: Environmental*. 2017; 209: 530-542. doi: 10.1016/j.apcatb.2017.02.072
34. Dar MA, Kim YS, Kim WB, et al. Structural and magnetic properties of CuO nanoneedles synthesized by hydrothermal method. *Applied Surface Science*. 2008; 254(22): 7477-7481. doi: 10.1016/j.apsusc.2008.06.004
35. Sahai A, Goswami N, Kaushik SD, et al. Cu/Cu<sub>2</sub>O/CuO nanoparticles: Novel synthesis by exploding wire technique and extensive characterization. *Applied Surface Science*. 2016; 390: 974-983. doi: 10.1016/j.apsusc.2016.09.005

36. Li H, Ban L, Wang Z, et al. Regulation of Cu species in CuO/SiO<sub>2</sub> and its structural evolution in ethynylation reaction. *Nanomaterials*. 2019; 9(6): 842. doi: 10.3390/nano9060842
37. Wang W, Liu Z, Liu Y, et al. A simple wet-chemical synthesis and characterization of CuO nanorods. *Applied Physics A: Materials Science & Processing*. 2003; 76(3): 417-420. doi: 10.1007/s00339-002-1514-5
38. Raimondi F, Geissler K, Wambach J, Wokaun AF. Hydrogen production by methanol reforming: Post-reaction characterisation of a Cu/ZnO/Al<sub>2</sub>O<sub>3</sub> catalyst by XPS and TPD. *Applied Surface Science*. 2002; 189(1-2): 59-71. doi: 10.1016/S0169-4332(01)01045-5
39. Yang J, Yuling L, Penghe Z, et al. Chemical thermodynamic and catalytic mechanism analysis of Cu-BTC-derived CuO<sub>x</sub>/C catalyst for selective catalytic reduction (SCR). *Molecular Catalysis*. 2022; 531: 112710. doi: 10.1016/j.mcat.2022.112710
40. He ZH, Li CC, Yang SY, et al. Electrocatalytic CO<sub>2</sub> reduction to ethylene over CuO<sub>x</sub> boosting CO<sub>2</sub> adsorption by lanthanide neodymium. *Catalysis Science & Technology*. 2023; 13(23): 6675-6684. doi: 10.1039/d3cy00893b
41. Ji Y, Guan A, Zheng G. Copper-based catalysts for electrochemical carbon monoxide reduction. *Cell Reports Physical Science*. 2022; 3(10): 101072. doi: 10.1016/j.xcrp.2022.101072
42. Mu G, Mu D, Wu B, et al. Microsphere-like SiO<sub>2</sub>/MXene hybrid material enabling high performance anode for lithium ion batteries. *Small*. 2019; 16(3): 1905430. doi: 10.1002/smll.201905430
43. Feng X, Jiang K, Fan S, et al. A direct grain-boundary-activity correlation for CO electroreduction on Cu nanoparticles. *ACS Central Science*. 2016; 2(3): 169-174. doi: 10.1021/acscentsci.6b00022
44. Bertheussen E, Hogg TV, Abghoui Y, et al. Electroreduction of CO on polycrystalline copper at low overpotentials. *ACS Energy Letters*. 2018; 3(3): 634-640. doi: 10.1021/acsenenergylett.8b00092
45. Chen R, Su H, Liu D, et al. Highly selective production of ethylene by the electroreduction of carbon monoxide. *Angewandte Chemie International Edition*. 2019; 132(1): 160-166. doi: 10.1002/ange.201910662
46. Coelho FMB, Botelho AM, Ivo OF, et al. Volumetric mass transfer coefficient for carbon monoxide in a dual impeller stirred tank reactor considering a perfluorocarbon–water mixture as liquid phase. *Chemical Engineering Research and Design*. 2019; 143: 160-169. doi: 10.1016/j.cherd.2019.01.013
47. Grosse P, Yoon A, Rettenmaier C, et al. Dynamic transformation of cubic copper catalysts during CO<sub>2</sub> electroreduction and its impact on catalytic selectivity. *Nature Communications*. 2021; 12(1): 6736. doi: 10.1038/s41467-021-26743-5
48. Yang PP, Zhang XL, Liu P, et al. Highly enhanced chloride adsorption mediates efficient neutral CO<sub>2</sub> electroreduction over a dual-phase copper catalyst. *Journal of the American Chemical Society*. 2023; 145(15), 8714-8725. doi: 10.1021/jacs.3c02130
49. Guo PP, He ZH, Yang SY, et al. Electrocatalytic CO<sub>2</sub> reduction to ethylene over ZrO<sub>2</sub>/Cu-Cu<sub>2</sub>O catalysts in aqueous electrolytes. *Green Chemistry*. 2022; 24(4): 1527-1533. doi: 10.1039/d1gc04284j

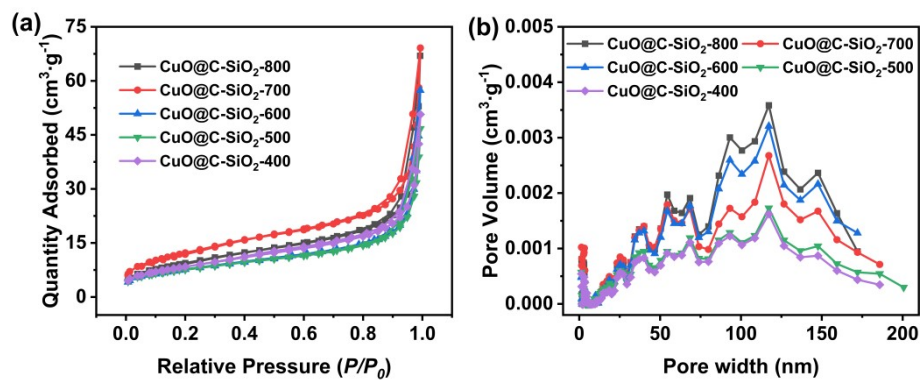
## Appendix



**Figure A1.** SEM images of catalysts: (a) CuO@C-SiO<sub>2</sub>-400, (b) CuO@C-SiO<sub>2</sub>-500, (c) CuO@C-SiO<sub>2</sub>-600, (d) CuO@C-SiO<sub>2</sub>-700, and (e) CuO@C-SiO<sub>2</sub>-800.



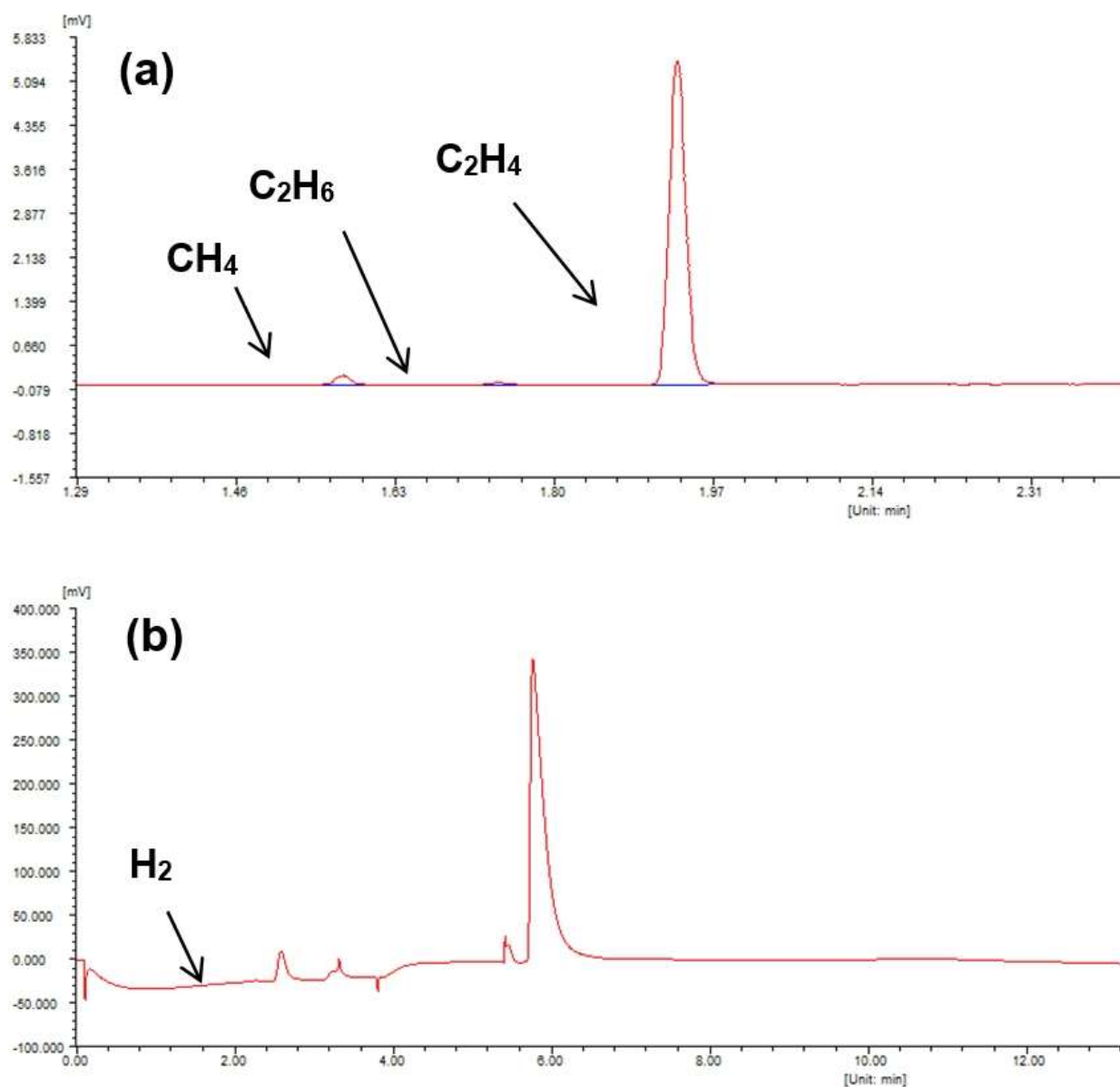
**Figure A2.** XRD patterns of CuO@C-SiO<sub>2</sub>-500 catalyst before and after reaction.



**Figure A3.** CuO@C-SiO<sub>2</sub>-X samples calcined at diverse temperatures: (a) N<sub>2</sub> adsorption/desorption isotherms and (b) pore size distribution curves.

**Table A1.** Results of N<sub>2</sub> adsorption-desorption isotherms.

Entry	Catalyst	BET surface area (m <sup>2</sup> ·g <sup>-1</sup> )	Mean pore size (nm)	Pore volume (cm <sup>3</sup> ·g <sup>-1</sup> )
1	CuO@C-SiO <sub>2</sub> -400	31	10	0.08
2	CuO@C-SiO <sub>2</sub> -500	28	10	0.07
3	CuO@C-SiO <sub>2</sub> -600	28	13	0.09
4	CuO@C-SiO <sub>2</sub> -700	45	10	0.11
5	CuO@C-SiO <sub>2</sub> -800	35	12	0.10

**Figure A4.** GC spectra of obtained products of C<sub>2</sub>H<sub>4</sub>, C<sub>2</sub>H<sub>6</sub>, CH<sub>4</sub>, and H<sub>2</sub> from CuO@C-SiO<sub>2</sub>-500 catalyst.

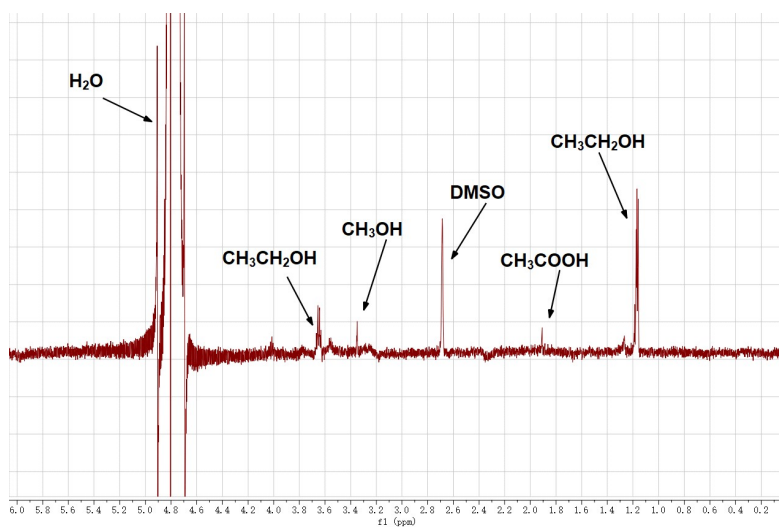


**Figure A5.**  $^1\text{H}$  NMR spectrum of liquid products from  $\text{CuO}@C\text{-SiO}_2\text{-500}$  catalyst in  $0.1 \text{ mol}\cdot\text{L}^{-1}$  of KOH electrolyte.

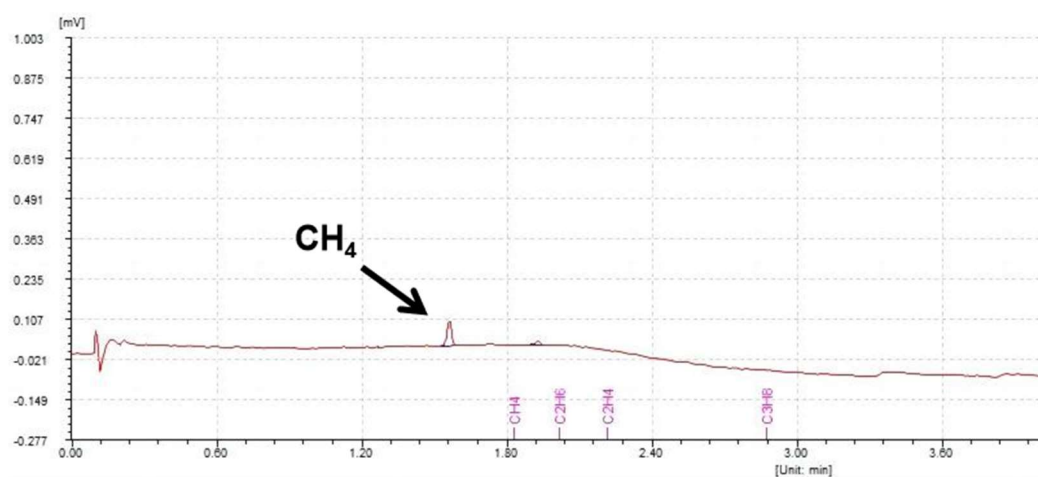


**Figure A6.** GC spectrum of obtained products from  $C\text{-SiO}_2$  catalyst.

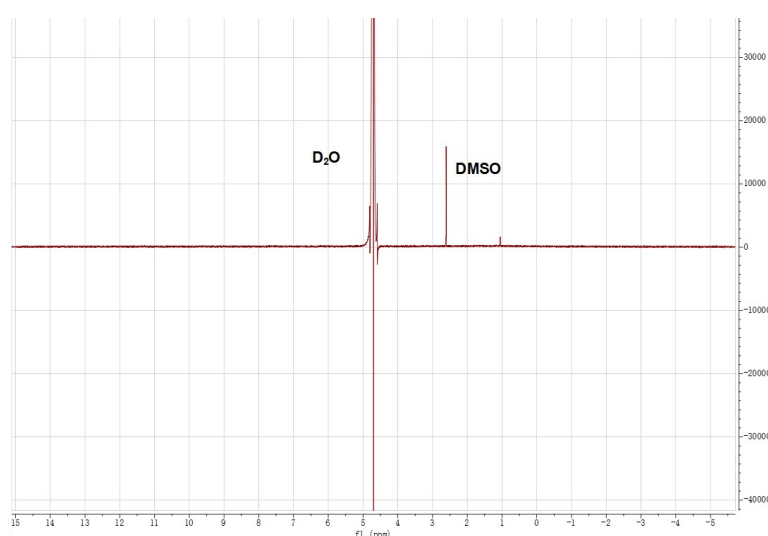


**Figure A7.**  $^1\text{H}$  NMR spectrum of liquid products from  $C\text{-SiO}_2$  catalyst in  $0.1 \text{ mol}\cdot\text{L}^{-1}$  of KOH electrolyte.

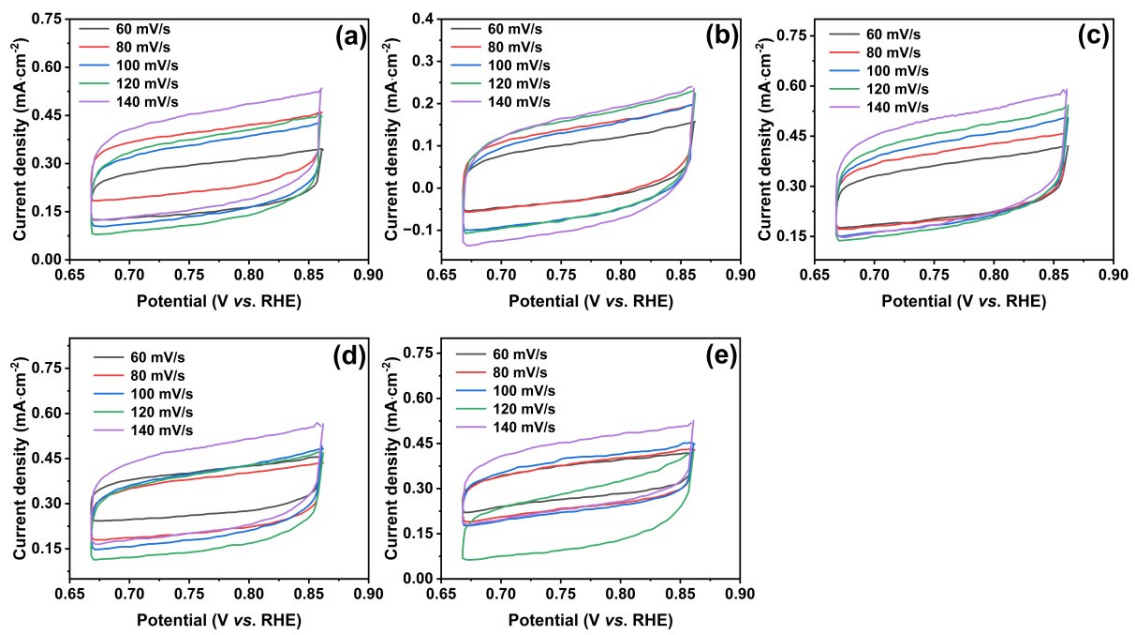


**Figure A8.** CV curves of catalysts calcinated at diverse temperatures of (a) 400 °C, (b) 500 °C, (c) 600 °C, (d) 700 °C, and (e) 800 °C at different scan rates in range of 0.668 V–0.861 V (vs. RHE).

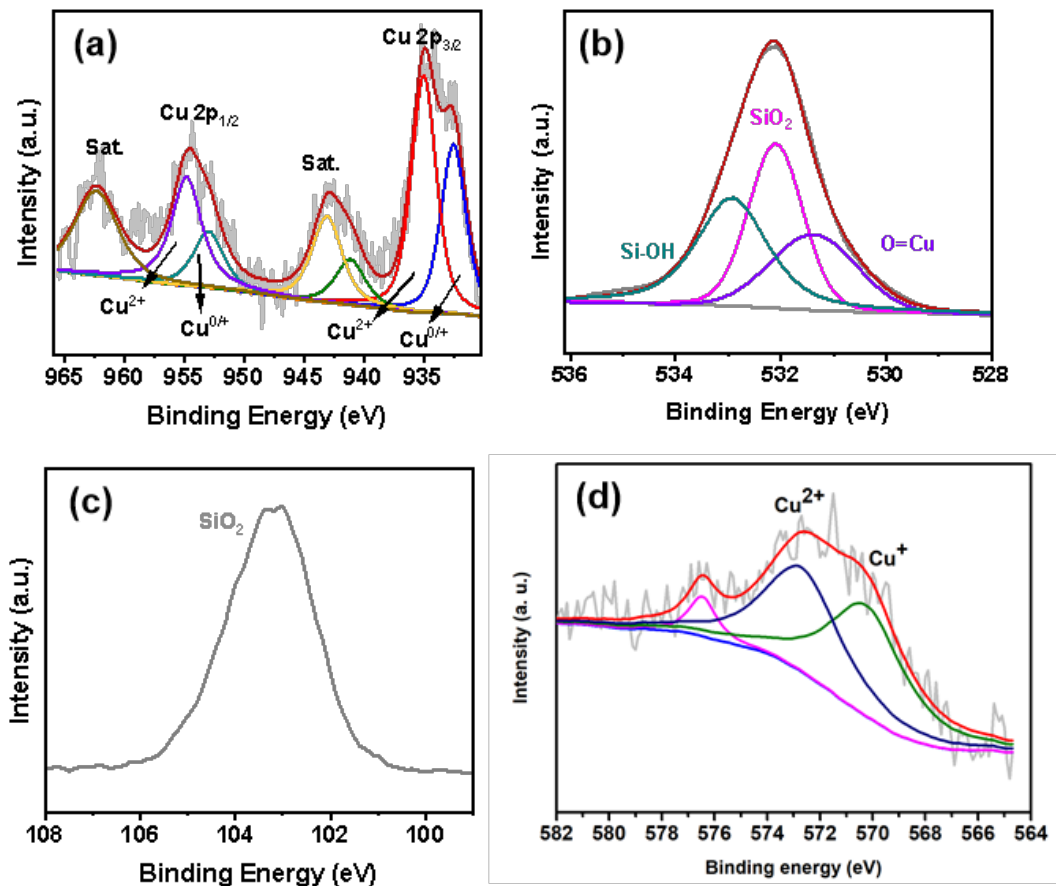


**Figure A9.** XPS spectra of the used CuO@C-SiO<sub>2</sub>-500 catalyst: (a) Cu 2p, (b) O 1s, (c) Si 2p, and (d) Cu LMM.

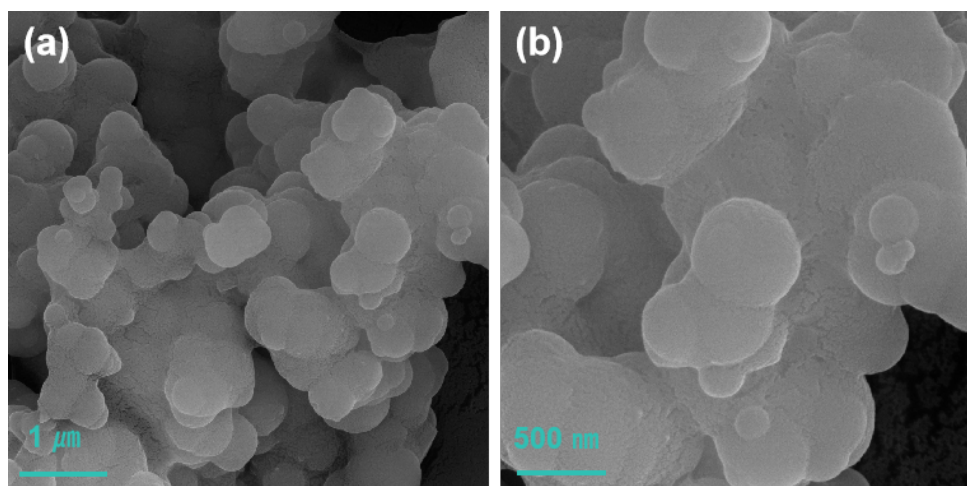


**Figure A10.** SEM images of the used CuO@C-SiO<sub>2</sub>-500.